ACS OMEGA

Open Access

http://pubs.acs.org/journal/acsodf

Article

Late Magmatic Activity in the Tarim Large Igneous Province: Evidence from the Puchang Granites

Zhuang Min, Zhengle Chen,* Jiayong Pan, Qing Zhang, Hailong Huo, Fengbin Han, Wengao Zhang, Xiaohu Wang, and Yu Wu

Cite This: *ACS Omega* 2023, 8, 47496−47509

Read Online

ACCESS | Metrics & More | Article Recommendations

ABSTRACT: The magmatic evolution sequence and tectonic activity background of the Permian Tarim large igneous province were discussed based on the research of petrogeochemistry, chronology, and zircon Lu−Hf isotope of two types of granite distributed in the Puchang V−Ti−magnetite deposit in the northwestern margin of Tarim. The results show that the two types are characterized by high silica, alkali, and potassium content. Both types of granites are enriched with light rare earth elements, including porphyritic granites with a negative anomaly of Eu and biotite monzogranites with a weak positive anomaly of Eu. The trace elements generally show that the large-ion lithophile elements are enriched relative to the high-field-strength elements, P and Ti are obviously depleted, and Rb, U, and K are relatively enriched. The zircon U−Pb age of porphyritic granites is 275.7 ± 1.0 Ma, the $\varepsilon_{Hf}(t)$ value ranges from −6.6 to −3.3, and the t_{DM2} ranges from 1469 to 1684 Ma. The zircon U−Pb age of biotite monzogranites is 268.9 ± 1.4 Ma. The $\varepsilon_{Hf}(t)$ value ranges from −1.2 to 0.5, and the t_{DM2} ranges from 1232 to 1340 Ma. The two types of granite were formed in a postcollisional extensional environment at the end of the early Permian, which is related to the Permian Tarim mantle activity and asthenosphere upwelling. The porphyritic granite was derived from an enriched lithospheric mantle; the biotite monzogranite was formed by the melting of mantle with crust contamination; and basalt and intrusive complexes in the research area were formed in an extensional intraplate rift environment.

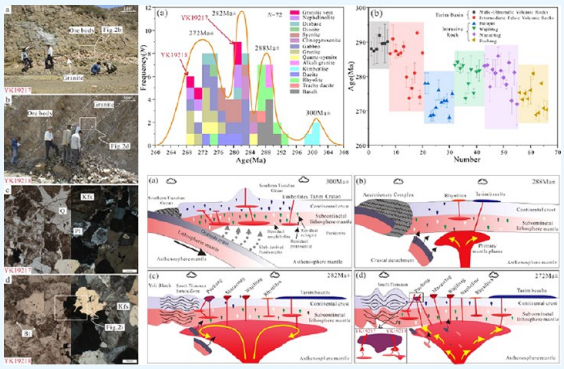

1. INTRODUCTION

The Tarim large igneous province (TLIP) is located in the northwest of Tarim Craton, which is surrounded by Tianshan, West Kunlun, and Altyn Tagh. The Tarim Craton was spliced on the Central Asian Orogenic Belt in the late Carboniferous.[1] In the early Permian, rifts occurred at the junction of the southern Tianshan mountains and Tarim to form alkalic basalt, alkalic gabbro−syenite-granite assemblages,[2] and late diabase and granites.[3] V−Ti-magnetite-mineralized intrusive complexes, such as Wajilitag and Puchang,[4−6] and Cu−Ni sulfide deposits, such as Karatungk and Huangshandong,[7,8] are believed to come from the partial melting of the Permian asthenosphere and metasomatic lithospheric mantle, respectively.[9] Halajun is one of the representative areas in the western section of the South Tianshan tectonomagmatic belt, which is mainly composed of Permian granitoids, followed by Permian volcanic rocks, intrusive complexes, syenites, granites, alkalic granites, and carbonatites among others. The granitic plutons, which are closely associated with layered ultramafic−mafic plutons, are formed by the crystallization and differentiation of intermediate-acidic melts differentiated by mafic magma and accompanied by different degrees of crustal mixing[10] or by partial melting of the Neoproterozoic gabbro source area.[11]

The Puchang complex is located in the northeast of Halajun, Keping thrust belt, northern margin of Tarim, the lithology of which is mainly medium-grained gabbro, and its metal minerals include titanomagnetite, ilmenite, and pyrrhotite. The resource quantities of iron and TiO_2 are medium-sized deposit, and the associated V_2O_5 resource is small.[12] Previous studies on geochemistry, Sr−Nb isotopes, and SHIMP zircon U−Pb chronology of gabbros in the Puchang complex indicate that partial melting under the subduction metasomatic lithospheric mantle source of the South Tianshan Ocean in the Early Mesozoic is a significant causality for the formation of the Puchang complex.[13−15] Based on the study of platinum group elements and the Re−Os of titanomagnetite, different degrees

Received: June 21, 2023
Revised: October 6, 2023
Accepted: October 17, 2023
Published: December 8, 2023

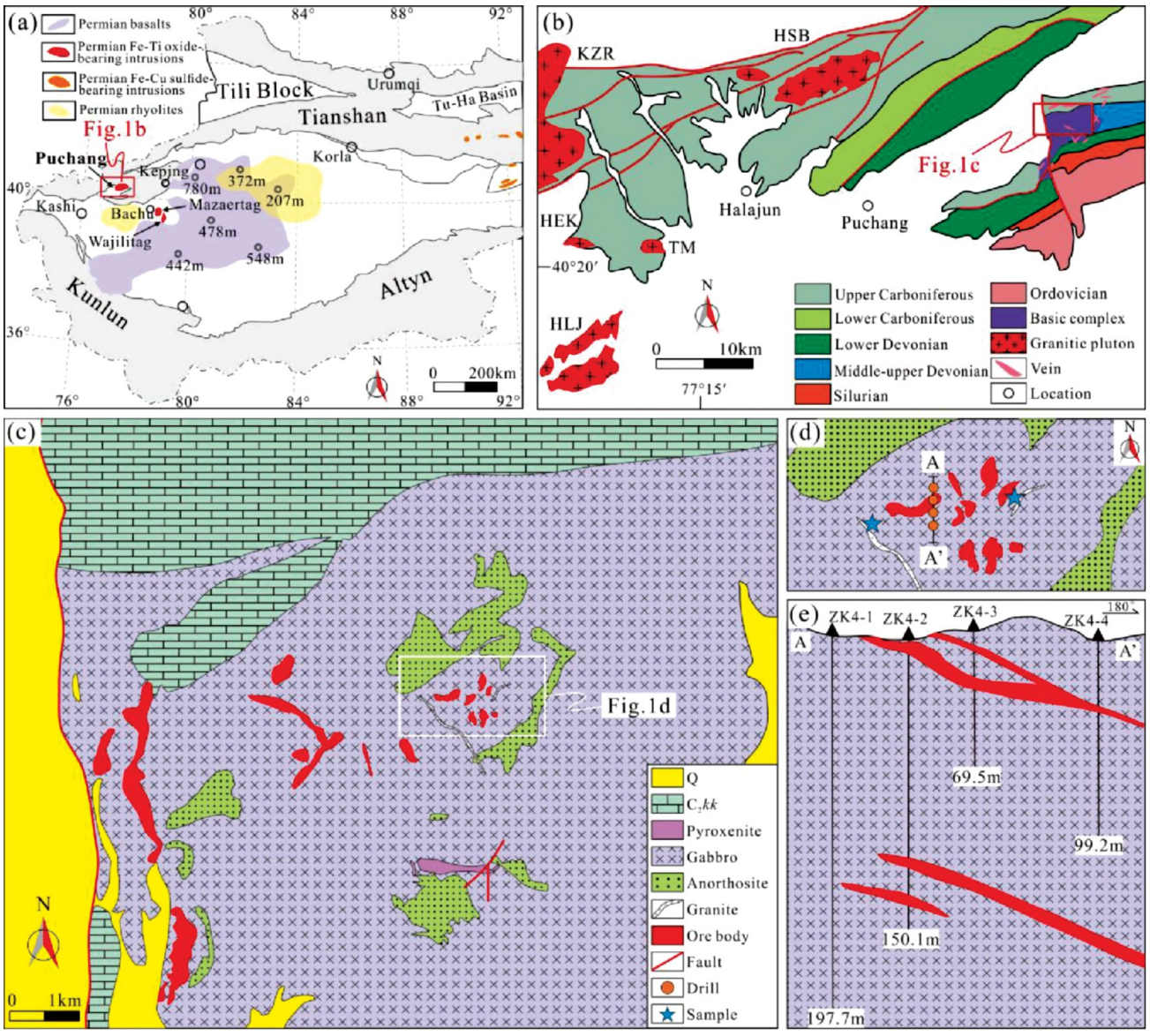

Figure 1. Geological maps of Puchang mining area (modified after Cao et al.[13]): (a) geological map of Tarim Basin; (b) geological structure map of Halajun; (c) geological map of Puchang V−Ti−magnetite area; (d) sampling location map; and (e) exploration line profile picture.

of crustal contamination are inferred to be the key factors leading to changes in sulfide saturation and segregation, along with the potential Cu−Ni sulfide deposits in the area[16,17] and the prospect of rare earth mineralization.[2] Many granites cut through strata, and plutons are developed in the mining area, but the genetic relationship among granites, intermediate-acid plutons, and ore-bearing complex and the relationship between granites and regional magmatic-tectonic evolution are undefined. This study investigates the petrogeochemistry, zircon U−Pb chronology, and zircon Lu−Hf isotopes of granites and discusses the regional magmatic evolution, metallotectonic setting, and metallogenetic epoch limitation, which is crucial for reconstructing the Permian magmatic activity history in the northern margin of Tarim.

2. REGIONAL GEOLOGY AND PETROGRAPHIC CHARACTERISTICS

The Tarim craton is mainly composed of Precambrian basement and Phanerozoic sedimentary cover.[18] The basement outcrops in Kuruktag and Aksu-Nantiekelike and is mainly composed of tonalite−trondhjemite−granodiorite assemblage.[19] The sedimentary strata of the Phanerozoic are mainly shallow marine and continental volcanic sedimentary strata. The rock assemblages associated with TLIP include ultramafic−mafic plutons, syenite, diabase, granite, trachyte, basalt, and rhyolite[20,21] (Figure 1a) represented by Puchang, Wajilitag, and Xiaohaizi, among other plutons related to V−Ti-magnetization.[2] Halajun is located in the intermediate zone of the Paleozoic shelf and Mesozoic fault uplift in Keping (Figure 1b) and is adjacent to Tiketage deep fault and Tianshan fold system in the north, the northwest edge of Tarim in the south, the north margin of Puchang sinistral strike-slip fault,[22] and the late Paleozoic Kuketale marginal basin.[23] The Cambrian−Ordovician Qiulitag, Ordovician Sargan, Silurian Kepingtag, Devonian Shalayim, Upper Carboniferous Kangkelin, and Lower Permian Belyakin Groups occur on the north of Halajun.[24] The ultramafic−mafic alkalic rocks, intermediate-acid alkalic rocks, and acid-alkalic-rich

https://doi.org/10.1021/acsomega.3c04415
ACS Omega 2023, 8, 47496−47509

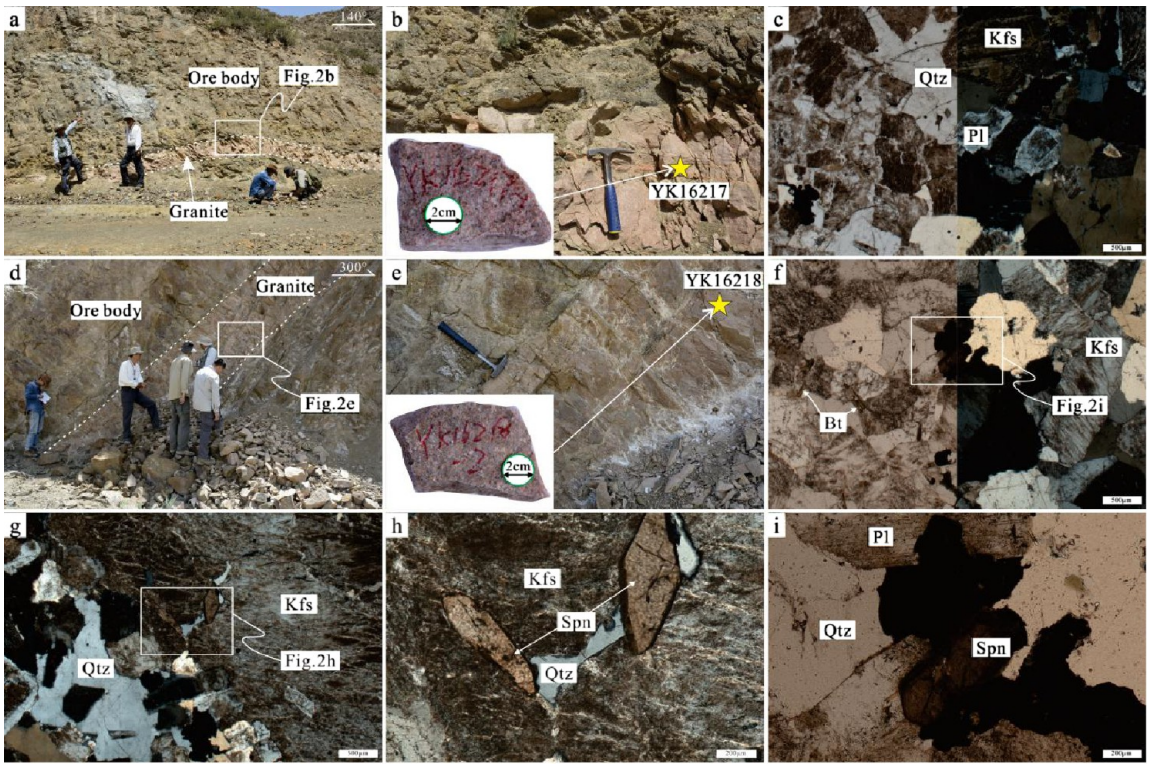

Figure 2. Field distribution and petrographic characteristics of Puchang granites: (a) the outcrop photo of YK16217; (b) the sample location of YK16217; (c) the mineral composition of YK16217; (d) the outcrop photo of YK16218; (e) the sample location of YK16218; (f) the mineral composition of YK16218; (g) the phenocryst is mainly composed of striped feldspar in YK16218; (h) the wedge sphene of YK16218; (e) the sample location of YK16218; and (i) the biotite and sphene of YK16217.

rocks are exposed, showing a set of mafic-acid rock assemblages, and the plutons are interspersed by late intermediate-acid granites.

The Upper Carboniferous Kangkelin Formation (C_2kk) limestone, intrusive complex, and granites are exposed in the mining area, among which the intrusive complex is embedded in carboniferous limestone (Figure 1c). The iron ore bodies occur in the midwest of the multistage emplaced intrusive complex and are distributed in the iron-bearing gabbro in the lower part of each rhythmic layer of the layered complex (Figure 1e). Gabbro is the main rock assemblage of ore-bearing plutons, and the crystalline grains range from coarse to fine-grained. Gabbro with different grain sizes present a gradual transition among each other, and the crystalline grains are distributed from coarse to medium-fine grained from northeast to southwest of the mining area. Coarse-grained gabbro has a large outcrop area with stable lithology and no mineralization. There are various titanomagnetite bodies of different rock types in medium-sized gabbro. A comprehensive geochemical anomaly body with Ti, Cu, and Co as the main ore-forming elements is developed on the surface, and the abnormal elements have a large distribution range, high content, and clear zoning, indicating the high ore-forming potential of this mining area.[25]

Several granites are observed in the midwestern part of the mining area (Figure 1d) and are pinkish in color and relatively fresh (Figure 2b). The granites tend toward NE with a dip angle ranging from 31 to 56° (Figure 2a,d). The largest one is 330 m long and 1−18 m thick, cutting through the complex bodies, which is a typical product of postmineralization magmatism (Figure 2a). According to their spatial distribution and lithologic differences, they can be divided into two categories. The first is flesh red medium coarse-grained porphyritic granite (YK16217) (Figure 2b) with a porphyritic structure (Figure 2g). The phenocryst is mainly composed of striped feldspar (particle size >1.0 mm) (Figure 2g), and the matrix is mainly composed of potassium feldspar (45−50%), plagioclase (20%±), and quartz (20−25%) (Figure 2c). The feldspar was generally clayized, with an occasional accessory mineral such as wedge sphene (Figure 2h). The second is a light red medium-fine biotite monzogranite (YK16218) (Figure 2f), and it has a local micrographic structure. It is mainly composed of potassium feldspar (35−40%), plagioclase (25%), quartz (25−30%), and biotite (5%±). A relatively fresh yellow-brown fine squamous biotite was commonly observed, whereas sphene and other accessory minerals were occasionally observed (Figure 2i).

3. SAMPLE COLLECTION AND ANALYSIS METHODS

As samples, three pieces of porphyry granites (YK16217) and three pieces of biotite monzogranites (YK16218) were collected from the mining area (Figures 1d and 2). The thin section, geochemical powder, and single mineral sorting were completed in Langfang Dikekantan Technology Service Co., Ltd. Zircon target making, transreflectance photography, and cathodoluminescence (CL) image acquisition were completed in Beijing Gaonianlinghang Technology Co., Ltd.

Rock geochemical analysis was performed at the National Geological Experimental Test Center of the Chinese Academy of Geological Sciences. The content of FeO was determined via a wet chemical method. The trace elements were determined by using a plasma mass spectrometer (PE300D).

https://doi.org/10.1021/acsomega.3c04415
ACS Omega 2023, 8, 47496−47509

Table 1. Major (%) and Trace ($\times 10^{-6}$) Element Compositions of the Puchang Granites[a]

Sample	16217-1	16217-2	16217-3	16218-1	16218-2	16218-3	Sample	16217-1	16217-2	16217-3	16218-1	16218-2	16218-3
SiO_2	72.41	72.09	72.06	73.45	73.42	72.51	Bi	0.08	0.20	0.05	0.08	0.08	0.10
Al_2O_3	14.91	15.07	14.77	14.37	14.36	14.53	Th	13.0	10.2	13.5	14.5	13.3	12.5
CaO	0.96	0.91	1.46	0.81	0.80	0.95	U	2.38	1.73	2.31	4.71	5.62	4.06
Fe_2O_3	0.58	0.14	0.45	0.78	0.68	0.96	Nb	16.1	15.2	16.5	10.9	11.1	10.5
FeO	0.54	0.90	0.22	0.47	0.61	0.36	Ta	2.04	2.03	2.03	1.49	1.46	1.56
K_2O	5.97	6.27	5.92	5.86	5.76	5.79	Zr	104	84.6	91.3	94.6	117	109
MgO	0.36	0.35	0.18	0.22	0.23	0.24	Hf	3.47	2.98	3.28	2.86	3.52	3.20
MnO	0.01	0.02	0.01	0.01	0.01	0.01	Ti	857	811	815	1067	1074	1131
Na_2O	4.10	4.08	3.91	3.73	3.75	3.82	W	0.43	0.39	0.48	0.48	0.50	0.57
P_2O_5	0.02	0.02	0.01	0.02	0.02	0.02	As	3.74	4.41	2.35	0.56	0.61	0.49
TiO_2	0.13	0.14	0.13	0.17	0.18	0.19	V	8.43	8.02	6.17	3.14	3.37	3.22
CO_2	0.12	0.05	0.10	0.12	0.10	0.10	Cr	1.12	1.01	0.84	0.97	0.98	1.21
H_2O^+	0.52	0.48	0.60	0.18	0.20	0.30	Sn	2.70	2.49	2.45	1.13	1.15	1.20
LOI	0.40	0.29	1.07	0.30	0.26	0.45	Sb	0.20	0.24	0.51	0.41	0.35	0.64
AR	1.32	1.33	1.31	1.30	1.29	1.30	La	26.9	25.3	26.9	27.1	28.2	25.1
ALK	10.07	10.35	9.83	9.59	9.51	9.61	Ce	51.2	47.6	48.4	42.0	43.5	39.4
A/CNK	1.35	1.34	1.31	1.38	1.39	1.38	Pr	5.92	5.77	5.22	4.48	4.45	4.03
$Mg^{\#}$	36.43	37.50	32.38	23.88	24.12	24.48	Nd	23.0	22.3	19.2	14.6	14.5	13.2
σ	3.45	3.68	3.33	3.02	2.97	3.13	Sm	5.34	5.08	4.04	2.21	2.12	1.98
T_{Zr}	743.32	727.05	732.99	735.79	752.84	753.12	Eu	0.85	0.78	0.80	0.76	0.73	0.79
Li	1.11	1.18	1.73	7.85	7.39	7.55	Gd	5.05	4.92	3.63	1.91	1.89	1.81
Be	2.84	2.25	2.21	2.82	2.89	2.75	Tb	0.83	0.85	0.61	0.30	0.31	0.29
Mn	68.3	69.6	60.6	53.4	61.4	64.9	Dy	4.89	4.95	3.42	1.79	1.72	1.68
Co	2.18	1.51	0.57	1.43	1.56	1.56	Ho	0.90	0.87	0.64	0.34	0.33	0.32
Ni	1.17	0.62	0.43	0.70	0.29	0.40	Er	2.44	2.30	1.70	0.96	1.02	0.90
Cu	3.53	2.41	2.08	2.23	1.66	1.90	Tm	0.35	0.32	0.27	0.15	0.16	0.15
Zn	23.8	22.8	11.7	12.3	13.0	13.7	Yb	2.12	2.00	1.63	1.07	1.09	1.05
Ga	17.1	17.1	16.8	14.9	15.6	15.9	Lu	0.28	0.26	0.22	0.18	0.19	0.17
Rb	139	172	164	184	183	184	Sc	3.38	2.87	2.65	1.78	1.75	1.65
Sr	129	138	130	139	142	151	Y	24.6	23.8	16.5	9.61	9.76	9.31
Mo	0.30	0.29	0.20	0.11	0.07	0.06	ΣREE	130.07	123.3	116.68	97.85	100.21	90.87
Cd	<0.05	<0.05	<0.05	<0.05	<0.05	<0.05	LREE/HREE	6.71	6.49	8.63	13.60	13.93	13.27
In	<0.05	<0.05	<0.05	<0.05	<0.05	<0.05	$(La/Yb)_N$	7.50	7.69	7.97	8.45	9.16	7.53
Cs	1.03	1.21	1.16	3.29	3.14	3.23	δEu	0.49	0.47	0.63	1.11	1.09	1.25
Ba	921	969	989	1506	1519	1609	Rb/Sr	1.08	1.25	1.26	1.32	1.29	1.22
Tl	0.40	0.42	0.39	0.63	0.65	0.64	Sr/Y	5.24	5.80	7.88	14.46	14.55	16.22
Pb	10.1	10.8	8.35	15.8	16.2	17.4	Sr/Yb	60.85	69.00	79.75	129.91	130.28	143.81

[a]A/CNK = $Al_2O_3/(CaO + Na_2O + K_2O)$ molecular number ratio; $(La/Yb)_N$, etc., are the normalized ratios of chondrites; T_{Zr} is the calculated result of the zirconium saturation temperature of the whole rock.

The mutual detection was performed using the plasma spectroscopy and chemical method, at an accuracy exceeding 5%.[11]

Zircon U−Pb chronology was completed at the State Key Laboratory of Ore Deposit Geochemistry, Institute of Geochemistry, Chinese Academy of Sciences. The laser denudation system (Coherent GeolasPro 193 nm) had a beam diameter of 32 μm and an energy density of 8.0 J/cm^2. An inductively coupled plasma mass spectrometer (Agilent 7700×) uses helium as carrier gas. Standard zircon 91500 (age 1065.4 ± 0.6 Ma)[26] was used as the external standard for matrix correction. Standard zircons GJ-1 (age 599.8 ± 4.5 Ma)[27] and Plešovice zircons (age 337.13 ± 0.37 Ma)[28] were used as blind samples and NIST SRM 610 as the external standard. Si was used as the internal standard to calibrate the content of Pb elements in zircon and Zr as the internal standard to calibrate the trace elements in zircon.[29] Data processing was completed using ICPMSDataCal 12.2 software.[30] U−Pb harmonics, age distribution frequency maps, and age weight-average calculation were performed using IsoplotR software.[31] For specific analysis methods and data processing, refer to related research studies.[30]

Zircon Hf isotopes were completed in Nanjing Polyspectral Detection Technology Co., Ltd. The laser denudation system (Analyte Excite 193 nm) has a beam spot diameter of 50 μm, an energy density of 6.0 J/cm^2, and a frequency of 8 Hz. Helium was used as a carrier gas in Nu Plasma II MC-ICP-MS. The Hf isotope target test points were delineated according to CL images and U−Pb age, and two standard zircons (including GJ-1, 91500, Plešovice, Mud Tank, and Penglai) were alternately tested for every 10 zircon samples to test the quality of zircon Hf isotope ratio data. $\varepsilon_{Hf}(t)$ was calculated using a ^{176}Lu decay constant of 1.867×10^{-11}a^{-1}.[32] The current ^{176}Hf/^{177}Hf and ^{176}Lu/^{177}Hf values of chondrites are 0.282772 and 0.0332, respectively.[33] The Hf isotope one-stage model age (T_{DM}) was calculated using the current depleted mantle ^{176}Hf/^{177}Hf and ^{176}Lu/^{177}Hf values of 0.28325 and 0.0384, respectively.[34] The mean crustal ^{176}Lu/^{177}Hf value used for the t_{DM2} was 0.015.[34] For detailed analysis methods and data processing, refer to the references.[35,36]

https://doi.org/10.1021/acsomega.3c04415
ACS Omega 2023, 8, 47496−47509

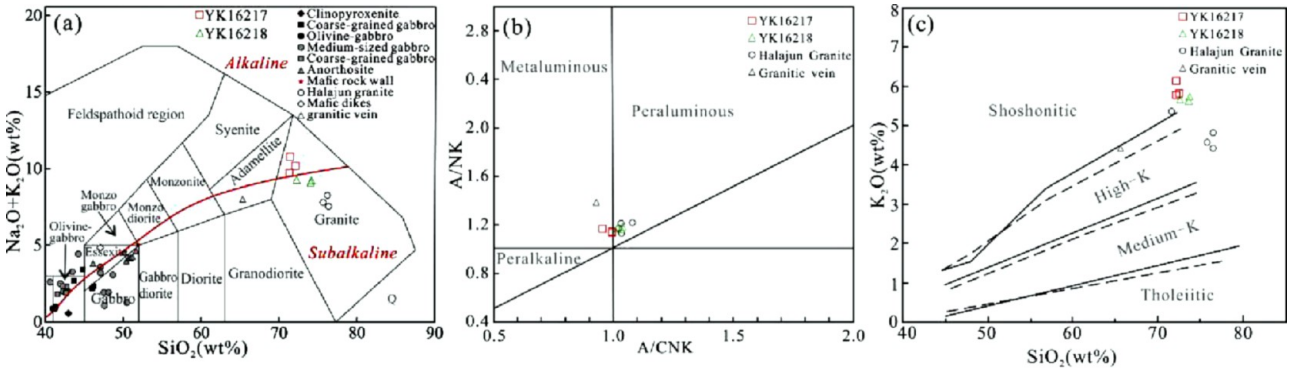

Figure 3. Diagram of rock geochemical classification of Puchang granites (data on intrusive complexes from Cao, 2015;[17] data on mafic dykes from Zhang et al., 2010;[24] and data on Halajun granites: mafic and granites from Zou, 2016:[37] (a) $Na_2O + K_2O$−SiO_2 (TAS) diagram[38] and (b) A/CNK−A/NK diagram;[39] and (c) K_2O−SiO_2 diagram[40]

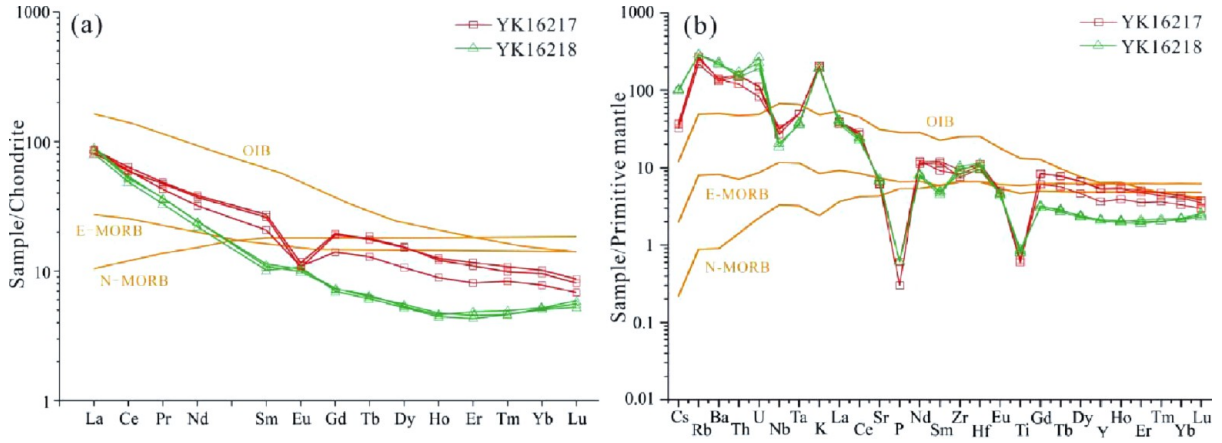

Figure 4. Diagram of rare earth elements and trace elements in Puchang granites (normalized values of rare earth elements from Boynton, 1984;[42] normalized values of trace elements from Sun and McDonough[43]): (a) the normalized rare earth element distribution pattern of chondrites and (b) The cobweb diagram of trace elements in the original mantle (E-MORB).

4. ANALYSIS RESULTS

4.1. Features of Major Elements. The sample of the Puchang granites was relatively fresh, and the data of the main elements are presented in Table 1. The average total alkali content (ALK) of porphyrinum granites was 10.08%. The average aluminum saturation index (A/CNK) was 1.33. The average value of $Mg^{\#}$ is 51.52. The average total alkali content (ALK) of biotite monzogranite was 9.57%. The average aluminum saturation index (A/CNK) was 1.38. The average value of $Mg^{\#}$ is 46.66. In the TAS diagram (Figure 3a), all of the data points fall in the granite area, the porphyritic granite is located in the alkalic area, and the biotite monzogranite is located in the subalkalic area. In the A/NK-A/CNK diagram (Figure 3b), it mainly falls in the transition region between metaluminous and peraluminous. In the SiO_2−K_2O diagram (Figure 3c), it falls within the transition region of the potassium calc-alkalic series. Compared with biotite monzogranite, porphyry granite has high Al_2O_3, CaO, FeO, MgO, Na_2O, H_2O, and LOI content and low SiO_2, Fe_2O_3, and TiO_2 content (ALK = $Na_2O + K_2O$; A/CNK = $Al_2O_3/(CaO + Na_2O + K_2O$; A/NK = $Al_2O_3/(Na_2O + K_2O)$; TAS is a scatter plot of the *Y*-axis is $(Na_2O + K_2O)$ and the *X*-axis is SiO_2).

Previous data showed that SiO_2 was from 55 to 65 wt % and distributed in the alkalic−subalkalic transition region (Figure 3). The alkali content $(Na_2O + K_2O)$ of the entire rock is positively correlated with SiO_2, reflecting that it is mainly controlled by the plagioclase, and $Fe_2O_3{}^T$ and TiO_2 are negatively correlated with SiO_2, while CaO and Al_2O_3 are positively correlated with SiO_2, which indicates that the entire rock composition is mainly influenced by the Fe−Ti oxide mineral content.[17,41] The distribution characteristics of major elements of granites are basically consistent with that in this study, while the granitic pluton has slightly lower K_2O and higher SiO_2 than the granites, which all have the characteristics of intraplate non-orogenic A-type granites.[37] The granites in the major and trace elements have undergone extensive crystal fractionation in the magma chamber or magmatic ascent and have distinguishable geochemical characteristics from the Puchang complex, which are likely to be derived from an OIB-like mantle source.[24]

4.2. Characteristics of Trace Elements. The average REE of porphyritic granite is 123.35×10^{-6}, the average ΣLREE/ΣHREE is 7.28, and the average $(La/Yb)_N$ is 10.0 for the LREE enrichment type (Figure 4a). The average δEu value is 0.54, indicating that plagioclase may remain in the source area. The average REE of biotite monzogranite is 96.31×10^{-6}. The average ΣLREE/ΣHREE is 13.60, and the average $(La/Yb)_N$ is 17.96, for the LREE enrichment type. The average δEu value is 1.17, which may be related to the separate crystallization of amphibole in the later magmatic evolution process. The HREE depletion indicates that garnet remains in the source area (REE represents the sum of 14 elements from

https://doi.org/10.1021/acsomega.3c04415
ACS Omega 2023, 8, 47496−47509

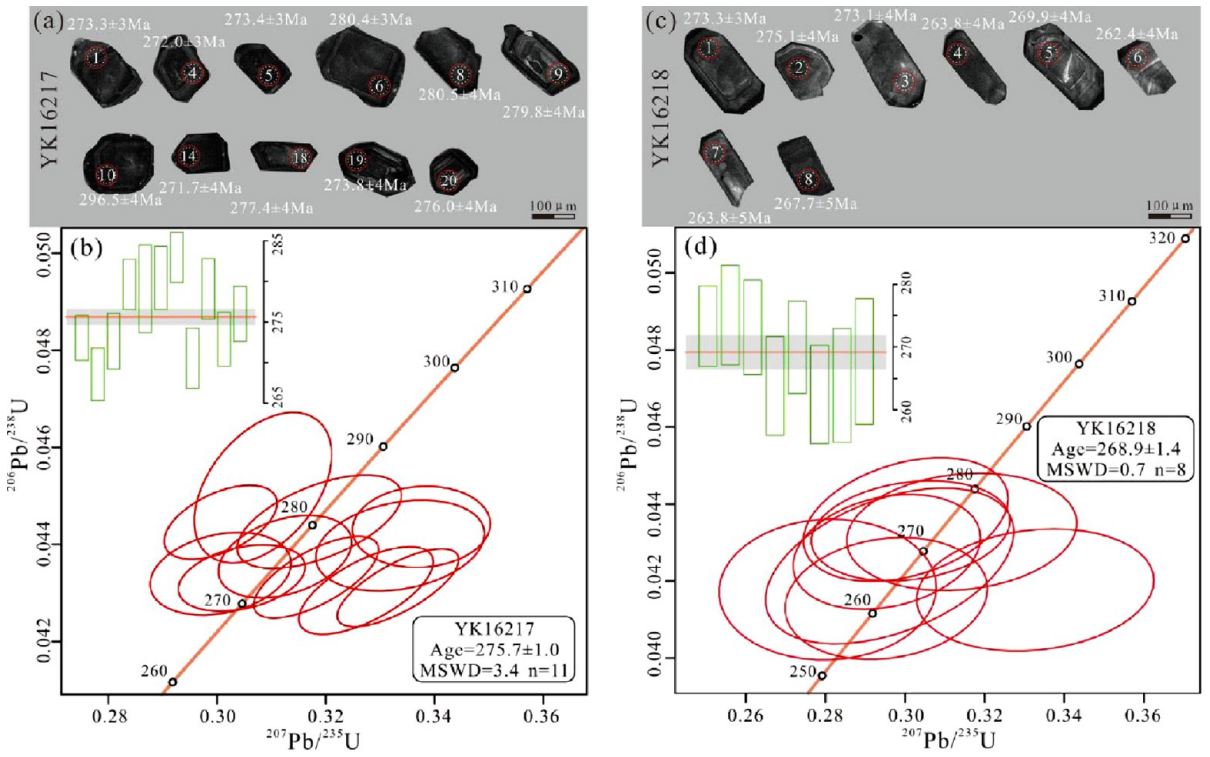

Figure 5. Concord diagram of the zircon U−Pb age of Puchang granites: (a) Cathode luminescence image of zircons from YK16217; (b) U−Pb concordia diagrams of zircons from YK16217; (c) cathode luminescence image of zircons from YK16218; and (d) U−Pb concordia diagrams of zircons from YK16218

La to Lu (Except Pm); LREE represents the sum of 6 elements from La to Eu (Except Pm); HREE represents the sum of 8 elements from Gd to Eu).

The spider diagram of standardized trace elements shows a right-leaning pattern (Figure 4b), which shows that it is generally rich in large-ion lithophile elements such as Cs, Rb, and K and high-field-strength elements such as Th and U and depletion of Nb, Ta, P, and Ti, indicating that the residual facies in the source region contain plagioclase, apatite, and possibly biotite, with the characteristics of mature continental arc granites.[44] Rb/Sr values ranged from 0.81 to 1.27, Rb/Nb values from 4.72 to 9.75, and the Nb deficit values from 0.4 to 0.6, which shows the characteristics of crust-derived magma. The fractional crystallization of rutile and ilmenite cannot reduce the Nb/Ta ratio of granites, while the fractional crystallization of amphibole and biotite or the fractional crystallization of Fe−Ti oxide may be the important mechanism of Nb/Ta differentiation of granites.[45] Combined with the geological and trace element characteristics of the deposit, Nb and Ta may enter the Fe−Ti-rich minerals crystallized by magma. Table 1 presents geochemical data.

4.3. Zircon Chronology. The zircons in porphyritic granites are mostly short columnar euhedral crystals and are translucent to opaque, with lengths ranging from 50 to 180 μm and widths ranging from 30 to 100 μm. The CL image shows that it has magmatic oscillatory bands (Figure 5a) with a Th/U ratio of 0.62−0.97, which is the characteristic of magmatic zircons.[46,47] In this study, 11 test points with a harmonicity of ≥90% were selected, and the average of U was 2026.87 × 10^{-6}. The average content of Th was 1464.77 × 10^{-6}. The $^{206}Pb/^{238}U$ age ranged from 271.7 to 296.5 Ma, with a weighted average age of 275.7 ± 1.0 Ma (mean squared weighted deviation (MSWD) = 3.4) (Figure 5c). The zircons in biotite monzogranites are mostly elongated columnar, colorless, and transparent, with fine mineral inclusions ranging 60−220 μm in length and 35−120 μm in width. CL images showed clear magmatic oscillatory bands (Figure 5b) with a Th/U ratio ranging from 0.50 to 0.69, which was the characteristic of magmatic zircons.[46,48] Then eight test points with a harmonicity of ≥90% were selected, and the average content of U was 484.51 × 10^{-6}. The average content of Th was 273.47 × 10^{-6}. The $^{206}Pb/^{238}U$ age ranged from 262 to 275 Ma, with a weighted average age of 268.9 ± 1.4 Ma (MSWD = 0.7) (Figure 5d). The Laser ablation inductively coupled plasma mass spectrometer (LA-ICP-MS) zircon U−Pb analysis data are listed in Table 2.

4.4. Zircon Hf Isotopes. Based on LA-ICP-MS zircon U−Pb chronology, the zircon Hf isotope data are shown in Table 3. The zircon $^{176}Yb/^{177}Hf$ ratio of porphyritic granites ranges from 0.1896226 to 0.0791814, and the $^{176}Hf/^{177}Hf$ ratio ranges from 0.282424803 to 0.282521543. The $\varepsilon_{Hf}(t)$ value ranges from −6.6 to −3.3. According to the average crustal $^{176}Lu/^{177}Hf$ value (0.015),[34] the single stage model age (t_{DM1}) ranged from 1063 to 1236 Ma and the t_{DM2} from 1469 to 1684 Ma. The $^{176}Yb/^{177}Hf$ ratio of zircon in biotite monzogranites ranged from 0.06506014 to 0.03153502 and the $^{176}Hf/^{177}Hf$ ratio from 0.28258153 to 0.282629717. The $\varepsilon_{Hf}(t)$ value ranged from −1.22 to +0.49. According to the average crustal $^{176}Lu/^{177}Hf$ value (0.015),[34] the single-stage model age (t_{DM1}) ranged from 872 to 954 Ma and the t_{DM2} from 1233 to 1340 Ma.

5. DISCUSSION

5.1. Magmatic Evolution Sequence. Past related research studies have chronologically examined the Puchang

https://doi.org/10.1021/acsomega.3c04415
ACS Omega 2023, 8, 47496−47509

Table 2. LA-ICP-MS Zircons U−Pb Dating Results of Puchang Granites

	ppm			isotope ratio								age (Ma)					
			Th	^{207}Pb		^{207}Pb		^{206}Pb		^{208}Pb		^{207}Pb		^{207}Pb		^{206}Pb	
Analysis	Th	U	U	^{206}Pb	1σ	^{235}U	1σ	^{238}U	1σ	^{232}Th	1σ	^{206}Pb	1σ	^{235}U	1σ	^{238}U	1σ
Porphyritic granite (YK16217)																	
1	2215.16	2509.78	0.88	0.0506	0.0013	0.3045	0.0077	0.0433	0.0005	0.0124	0.0002	220.4	59	269.9	6	273.3	3
4	1702.55	2744.02	0.62	0.0555	0.0011	0.3333	0.0074	0.0431	0.0005	0.0132	0.0002	431.5	46	292.1	6	272.0	3
5	3351.30	3774.75	0.89	0.0526	0.0011	0.3182	0.0076	0.0433	0.0006	0.0128	0.0002	322.3	48	280.5	6	273.4	3
6	1431.65	1983.19	0.72	0.0485	0.0011	0.3006	0.0069	0.0445	0.0005	0.0129	0.0002	124.2	52	266.9	5	280.4	3
8	986.18	1686.36	0.58	0.0494	0.0013	0.3084	0.0083	0.0452	0.0010	0.0138	0.0003	164.9	64	273.0	6	284.8	6
9	677.87	1020.49	0.66	0.0512	0.0015	0.3188	0.0100	0.0445	0.0006	0.0139	0.0003	250.1	69	281.0	8	280.5	4
10	2256.64	2473.99	0.91	0.0548	0.0015	0.3376	0.0084	0.0444	0.0006	0.0137	0.0003	405.6	61	295.3	6	279.8	3
14	1490.10	2299.85	0.65	0.0545	0.0012	0.3274	0.0082	0.0430	0.0006	0.0161	0.0004	390.8	50	287.6	6	271.7	4
18	738.93	1087.36	0.68	0.0548	0.0017	0.3337	0.0103	0.0440	0.0006	0.0144	0.0005	405.6	64	292.4	8	277.4	4
19	1069.10	1100.70	0.97	0.0500	0.0014	0.3006	0.0086	0.0434	0.0006	0.0131	0.0003	198.2	67	266.9	7	273.8	3
20	1856.82	2162.68	0.86	0.0516	0.0014	0.3125	0.0081	0.0437	0.0006	0.0138	0.0003	264.9	56	276.1	6	276.0	3
Biotite monzogranite (YK16218)																	
3	282.41	528.74	0.53	0.0474	0.0020	0.3014	0.0102	0.0433	0.0005	0.0137	0.0003	77.9	87	267.5	8	273.3	3
7	337.90	650.79	0.52	0.0497	0.0017	0.3002	0.0105	0.0436	0.0007	0.0137	0.0004	189.0	80	266.5	8	275.1	4
8	193.58	329.00	0.59	0.0527	0.0020	0.3142	0.0118	0.0433	0.0006	0.0133	0.0004	316.7	119	277.5	9	273.1	4
9	372.36	597.01	0.62	0.0578	0.0020	0.3327	0.0122	0.0418	0.0006	0.0138	0.0004	520.4	78	291.6	9	263.8	4
15	268.68	539.20	0.50	0.0496	0.0016	0.2954	0.0096	0.0428	0.0006	0.0130	0.0003	176.0	77	262.8	8	269.9	4
16	257.97	494.51	0.52	0.0512	0.0019	0.2953	0.0104	0.0415	0.0006	0.0127	0.0003	250.1	92	262.7	8	262.4	4
19	254.32	369.56	0.69	0.0483	0.0020	0.2806	0.0112	0.0418	0.0007	0.0131	0.0004	122.3	100	251.1	9	263.9	5
20	220.57	367.29	0.60	0.0493	0.0019	0.2961	0.0128	0.0424	0.0008	0.0125	0.0004	164.9	88	263.4	10	267.7	5

https://doi.org/10.1021/acsomega.3c04415
ACS Omega 2023, 8, 47496−47509

Table 3. Zircon Hf Isotopic Compositions of Puchang Granites

Analysis	t (Ma)	$^{176}Yb/^{177}Hf$	1σ	$^{176}Lu/^{177}Hf$	1σ	$^{176}Hf/^{177}Hf$	1σ	$\varepsilon_{Hf}(t)$	t_{DM1}	t_{DM2}	$f_{Lu/Hf(s)}$
Porphyritic granite (YK16217)											
1	280.8	0.1896226	0.002250	0.0046520	0.000055	0.2824625	0.000011	−11.40	1235	1652	−0.00060274
2	280.8	0.0861787	0.000769	0.0021986	0.000016	0.2824575	0.000008	−11.58	1160	1635	−0.00057481
3	280.8	0.1003930	0.001660	0.0025488	0.000041	0.2824382	0.000009	−12.26	1199	1682	−0.00064961
4	280.8	0.1254529	0.000818	0.0033173	0.000030	0.2824692	0.000011	−11.17	1179	1622	−0.00055421
5	280.8	0.1579612	0.000525	0.0039070	0.000013	0.2824707	0.000010	−11.11	1197	1625	−0.00055987
6	280.8	0.1018068	0.001050	0.0024044	0.000024	0.2825120	0.000007	−9.65	1087	1516	−0.00038579
7	280.8	0.1181163	0.001310	0.0029768	0.000035	0.2824567	0.000010	−11.61	1186	1646	−0.00059211
8	280.8	0.1163617	0.001240	0.0027694	0.000031	0.2825361	0.000007	−8.80	1063	1467	−0.00030730
9	280.8	0.1031526	0.000681	0.0025658	0.000018	0.2824986	0.000009	−10.13	1112	1548	−0.00043620
10	280.8	0.1602821	0.001080	0.0039826	0.000030	0.2824613	0.000012	−11.45	1214	1647	−0.00059454
11	280.8	0.1398693	0.001270	0.0034729	0.000035	0.2825099	0.000009	−9.73	1123	1533	−0.00041309
12	280.8	0.0791814	0.000509	0.0020492	0.000014	0.2824730	0.000009	−11.03	1133	1599	−0.00051718
Biotite monzogranite (YK16218)											
1	268.9	0.0608669	0.000619	0.001560	0.000014	0.282589	0.000009	−6.92	952	1340	−0.00012158
2	268.9	0.0363110	0.000331	0.000947	0.000008	0.282588	0.000008	−6.98	939	1337	−0.00011696
3	268.9	0.0397183	0.000291	0.001050	0.000007	0.282593	0.000009	−6.79	934	1327	−0.00009969
4	268.9	0.0619908	0.000384	0.001710	0.000009	0.282636	0.000008	−5.27	889	1238	0.00004103
5	268.9	0.0359683	0.000198	0.000959	0.000006	0.282634	0.000010	−5.36	875	1235	0.00004522
6	268.9	0.0315350	0.000201	0.000851	0.000005	0.282634	0.000007	−5.34	872	1233	0.00004892
7	268.9	0.0628455	0.001080	0.001560	0.000025	0.282621	0.000008	−5.81	907	1270	−0.00001080
8	268.9	0.0417546	0.000271	0.001110	0.000007	0.282600	0.000007	−6.55	926	1312	−0.00007635
9	268.9	0.0416478	0.000648	0.001130	0.000014	0.282602	0.000009	−6.48	924	1308	−0.00007026
10	268.9	0.0650601	0.000421	0.001740	0.000011	0.282592	0.000010	−6.84	954	1338	−0.00011738
11	268.9	0.0326991	0.000190	0.000858	0.000005	0.282598	0.000008	−6.60	922	1313	−0.00007753
12	268.9	0.0344586	0.000345	0.000905	0.000004	0.282589	0.000011	−6.93	936	1334	−0.00011163

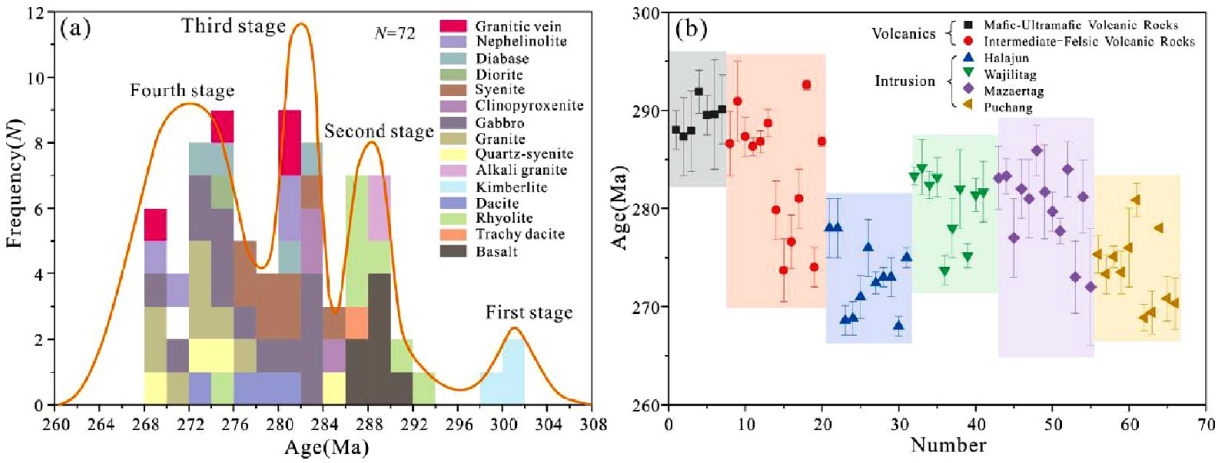

Figure 6. Statistical distribution map of the chronology of magmatic rocks in the northern margin of Tarim: (a) the age histogram of magmatic rocks in the northern margin of Tarim and (b) The error map of age distribution of different geological bodies.

mining area; for example, the U−Pb zircon dating of gabbro in the Puchang complex was performed using LA-ICP-MS and Sensitive High Resolution Ion Microprobe (SHRIMP), and the results were 262 ± 2 Ma and 276 ± 4 Ma, respectively.[49] The $^{49}Ar-^{39}Ar$ plateau age of plagioclase in gabbro was 265.5 ± 1.2 Ma, and the corresponding isochron age was 267.29 ± 5.62 Ma. On the basis of the stratigraphic paleontological evidence, the Puchang plutons and Kupkurtzman basalts belong to the early Middle-Permian Magmatism.[50] The U−Pb ages of zircons in gabbros and ores obtained by SIMS ranged from 273 to 275 Ma, and the U−Pb ages of LA-ICP-MS zircons are 275.1 ± 1.1 Ma.[51] The ages of Puchang gabbros are consistent with those of TLIP and show multistage mineralization.[52] SHRIMP zircon U−Pb age of gabbro samples from the Puchang complex ranged from 269.4 ± 2.2 Ma.[17] The study results show that the crystalline ages of porphyry granites and hosting rocks are consistent within the error range and are the products of the near synchronous magmatic activity. The biotite monzogranite was formed significantly later than the porphyritic granite, which is related to the latest magmatic activity in the northern margin of Tarim (Figure 6a) and constrains the lower limit of the mineralization age of Puchang V−Ti-magnetite.

Previous studies have shown that the magmatic rocks in the TLIP can be roughly divided into basalts (290−285 Ma) in the early period, ultramafic−mafic intrusive rocks, and syenite intrusive rocks (284−274 Ma) in the late period.[53] Time series mapping informed by the detailed evaluation and screening of

https://doi.org/10.1021/acsomega.3c04415
ACS Omega 2023, 8, 47496−47509

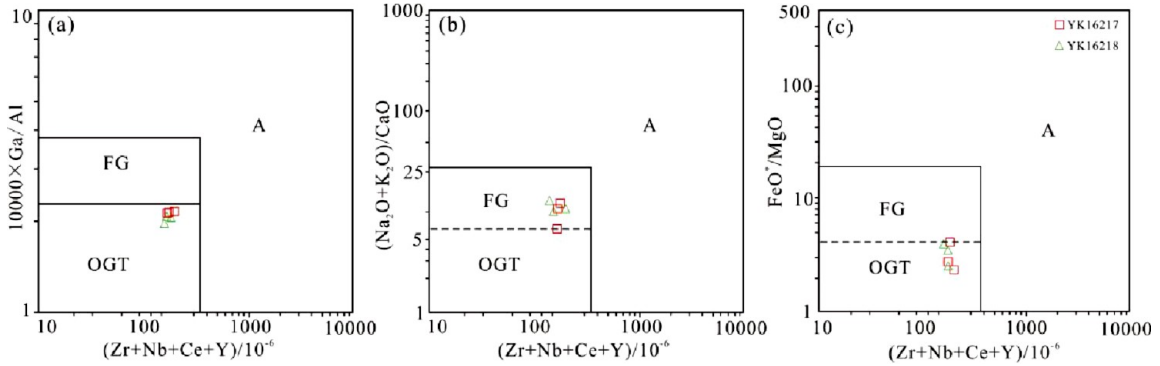

Figure 7. Diagram of genetic identification of Puchang granites (FG: highly differentiated granite and OGT: undifferentiated granite) (according to Whalen et al.[59] and Eby[60]): (a) (Zr + Nb + Ce + Y)−10 000 × Ga/Al discrimination diagram; (b) (Na2O + K2O)/CaO (Zr + Nb + Ce + Y) discrimination diagram; and (c) FeO*/MgO—(Zr + Nb + Ce + Y) discrimination diagram.

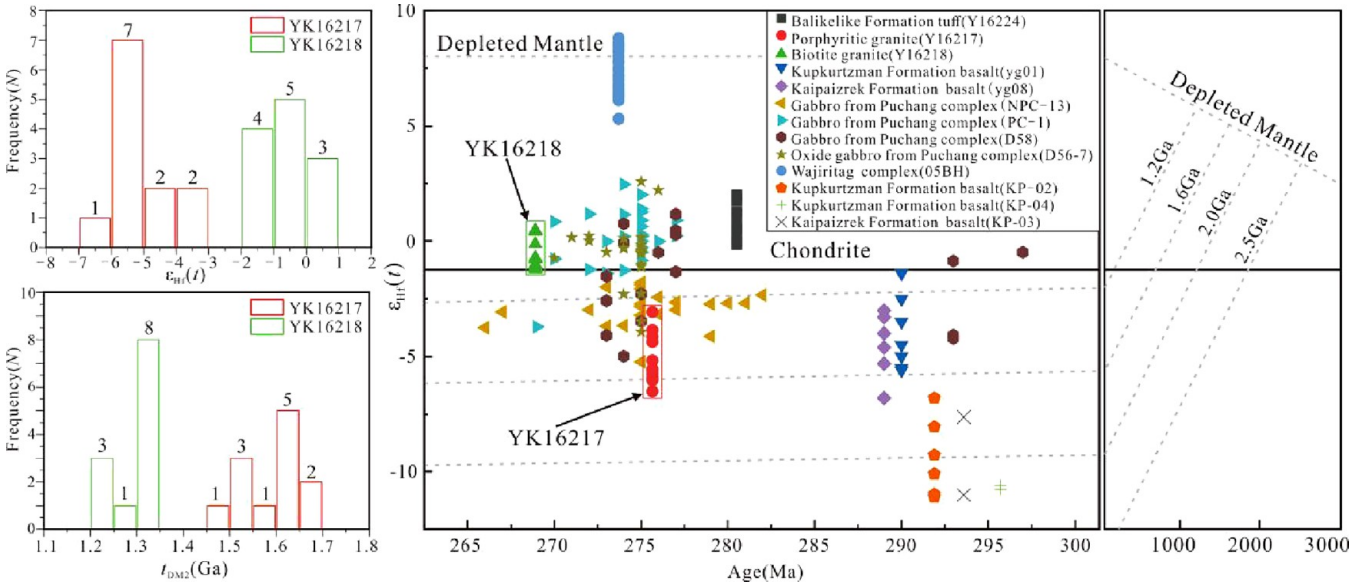

Figure 8. Zircon Hf isotopic composition in Puchang granites (Y16224 is unpublished data of the project team; yg01 and yg08 data from Li;[61] NPC-13, PC-1, D58, and D56-7 from Zhang et al.;[51] 05BH data from Zhang et al.;[62] KP-02, KP-03, and KP-04 from Zhang et al.[11]).

the age data of the early Permian magmatic rocks in Tarim yielded four periods of magmatic events in the TLIP: the first stage is characterized by the formation of kimberlite dykes;[12] the second stage is dominated by continental flood basalt and rhyolite, which are mainly supplied by the melting of lithospheric mantle and crustal materials, respectively, and are the products of the continuous interaction between mantle plume and lithospheric mantle;[54] and the third stage is dominated by pyroxenite, gabbro, and syenite, followed by diorite, diabase, and granite, which is the main period of magma formation in the area.[17] Furthermore, the fourth stage shows nephelinolite and alkalic granite, followed by the latest alkalic intrusion.[16] There are significant differences among different types of rock associations and age distributions in different regions (Figure 6b). The volcanic rocks in the northern margin of the Tarim uplift belt were formed earlier, where the eruption of intermediate acid volcanic rocks lasted longer, followed by the formation of Wajilitag and Xiaohaizi plutons, and the magmatic activity in the Halajun region was relatively late (Figure 6b). The age statistics here show that the magmatic pulsation has multiple phases and stages and does not represent a strict limit of the diagenetic age. The relatively long time span of magmatic activity (about 30 Ma) indicates that the Permian Tarim magmatite was formed under the background of a long-term active mantle plume.

5.2. Crust−Mantle Interaction. Granites can be divided into I-type, S-type, M-type, and A-type granites according to their source area properties.[55] The average A/CNK value of Puchang granites is 1.36, $K_2O > Na_2O$, trace element composition, inherited zircon, and other characteristics, which can exclude the M-type granite type of a new mantle source material. A-type granite contains alkalic dark-colored minerals and is characterized by rich Si, K and Zr, Nb, Ta in chemical composition. The values of 10 000 × Ga/Al and Zr + Nb + Ce + Y of granites are 2.6 × 10^{-6} and 350 × 10^{-6}, respectively. The content of SiO_2 is low (<74%), the value of Al_2O_3/TiO_2 ranges from 76.47 to 114.69, and the value of CaO/Na_2O is low (<0.24). Generally, FeO*/MgO of the samples is relatively low (4.18 on average), and the content of Zr + Nb + Ce + Y is relatively low, and there is no mafic hornblende and other characteristic minerals, so the samples do not belong to A-type granites. In the discriminant diagram of (Zr + Nb + Ce + Y) − 10 000 × Ga/Al (Figure 7a), the data points are located in the "undifferentiated granite" and in the

https://doi.org/10.1021/acsomega.3c04415
ACS Omega 2023, 8, 47496−47509

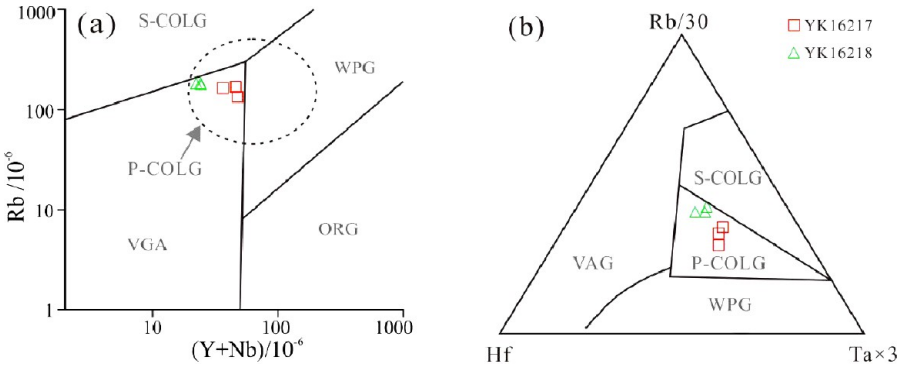

Figure 9. Discrimination diagram of a tectonic environment of Puchang granites: (a) Rb/30−Hf−Ta × 3 diagram and (b) Rb-(Yb + Ta)/10^{-6} diagram.

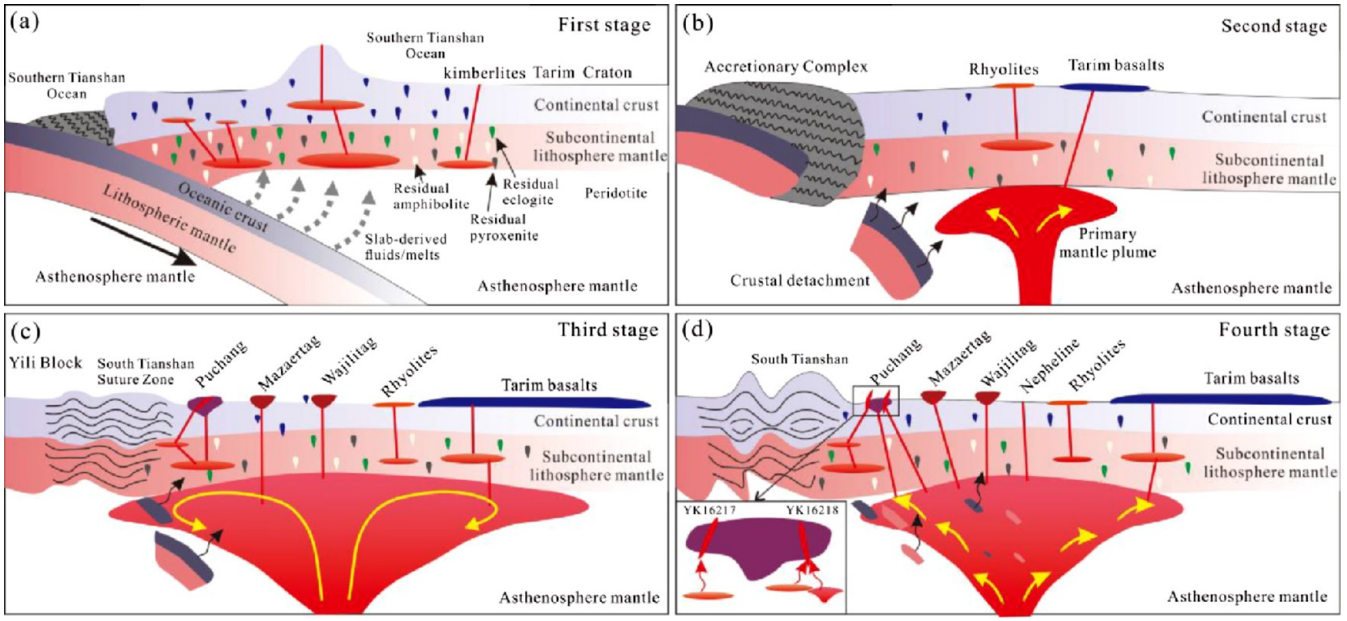

Figure 10. Metallogenic pattern of Puchang granites: (a) interaction between SCLM and subducting oceanic material; (b) TLIP basalt and rhyolite; (c) origin of the Fe−Ti oxide ore intrusive complex; and (d) nepheline and schematic of the formation of granites.

comprehensive diagram of $(Na_2O + K_2O)/CaO - (Zr + Nb + Ce + Y)$ and $FeO^*/MgO - (Zr + Nb + Ce + Y)$ (Figure 7b, Figure 7c). The samples are mainly categorized under FG and OGT. Typical S-type granites often refer to strong peraluminous granitoids containing cordierite. Muscovite and garnet are not effective markers for the identification of S-type granites.[56] Previous studies have pointed out that P has high solubility in strong peraluminous melt and low solubility in aluminized or weak peraluminous melt;[57] the sample has a very low P_2O_5(<0.1%).[58] The A/CNK values range from 0.95 to 1.04, which is obviously different from typical peraluminous S-type granites. Therefore, the Puchang granites should be categorized under weak peraluminous I-type granites, which have undergone some degrees of differentiation.

Zircon Hf isotope is often used to investigate granitic provenance. Positive values of $\varepsilon_{Hf}(t)$ can be interpreted as the melting of new crust or the addition of mantle materials, while negative values can be interpreted as the remelting of old crust materials.[47] As previously mentioned, the porphyritic granite has a relatively low $\varepsilon_{Hf}(t)$ value ranging from −6.50 to −3.07 and the t_{DM2} ranges from 1466 to 1681 Ma; The biotite monzogranite has a high initial value of $^{176}Hf/^{177}Hf$, positive $\varepsilon_{Hf}(t)$ values ranging from −1.22 to 0.49, and the t_{DM2} ranging from 1232 to 1340 Ma. The difference between $\varepsilon_{Hf}(t)$ and t_{DM2} values indicates that the two granites have different contribution ratios from those of the source region. The variation range of $\varepsilon_{Hf}(t)$ in the Puchang complex is between the two types of granite.[16] The results of past related studies and regional data indicate the presence of mantle-derived magma intrusion events; a small amount of mantle material may be involved in the formation of granites, porphyritic granites may come from the enriched mantle (that is, the ancient material circulation or transformation), and biotite monzogranites come from a small amount of depleted mantle but mainly from the reworking and recycling of pre-existing crustal components. The Hf isotope data of zircons from different lithologies show that the Hf isotope values are mainly negative in the early stage and close to positive in the late stage, indicating that the upwelling Tarim mantle plume is continuously injecting the depleted mantle material into the magma source area of the TLIP and continuously changing the isotopic composition of the latter to gradually evolve to the depleted mantle source area (Figure 8). Moreover, a series of

https://doi.org/10.1021/acsomega.3c04415
ACS Omega 2023, 8, 47496−47509

rock assemblages with continuous evolutionary trends in isotopic characteristics were formed.[61]

5.3. Mantle Plume and Magmatic Activity. The Permian intermediate-acid magmatic rock belt developed in the northwest margin of the Tarim Basin is considered by predecessors to be the product of the "A-type" subduction from the Tianshan arc to the Tarim block in the middle Permian.[45] Based on the comprehensive study of paleontology and paleomagnetism, the Tarim block may have formed a complex orogenic accretionary belt in the late Permian middle Triassic and the Middle Tianshan Yili block,[63] while the accretionary wedge formed in Inner Mongolia and adjacent areas along the southern part of the Siberian active margin and the northern part of the active margin of the North China Craton may reach the Middle Triassic.[64] However, some scholars believe that the collision of the western segment of the South Tianshan orogenic belt occurred relatively later than the eastern segment in the Late Carboniferous, and the Permian Triassic zircon ages in metamorphic rocks may be the result of late crustal hydrothermal events.[1] In recent years, domestic scholars have extensively studied the Permian TLIP, mainly believing that the area was in an intracontinental extensional environment in the Permian, and large-scale flood basalt and magmatic intrusion were related to mantle plume activities.[65−68] Recently, certain scholars have focused on the geochemical study of the magmatic rocks of Tarim and Western Tianshan (330−360 Ma) and proposed that the northern margin of the Tarim resulted from the interaction between the mantle plume and orogeny during the Permian period.[68] In the Rb/30−Hf−Ta × 3 diagram (Figure 9b), the sample points are relatively concentrated, showing the characteristics of granites in the postcollision environment. In the Rb- $(Yb+Ta)/10^{-6}$ diagram (Figure 9a), it is classified under the postcollision environment area, which is relatively close to the cocollision area and belongs to the products of magmatic activities in the late orogenic or postorogenic period.

The Permian magmatism in the northern margin of Tarim was mainly affected by the closure of the Tianshan Ocean and the Tarim mantle plume. The specific evolution model is as follows: (1) At the end of the Carboniferous (first stage), the southern Tianshan oceanic crust continued to subduct northward under the Tarim craton, and this process constantly metasomatized the enriched subcontinental lithospheric mantle (SCLM), resulting in the low-degree melting of the volatile mantle to form the Wajilitag kimberlite and Tarim large volcanic province among others (Figures 6b and 10a). These rocks and minerals retain information about their mantle origin (SCLM). There is no evidence that the Tarim mantle was formed and directly formed these rocks at this time. (2) In the early Permian (second stage), the subduction of the southern Tianshan oceanic crust stopped and delamination occurred. The mantle plume formed and invaded the bottom of the Tarim lithospheric mantle. The lithospheric mantle was partially melted to form rhyolite. At the same time, the interaction between the mantle plume and lithospheric mantle erupted to form an overflow basalt (Figure 10b). (3) In the early Permian (third stage), after a large area of basalt eruption, the Tarim mantle plume grew laterally and continued to rise, causing adiabatic decompression and partial melting at the top of the mantle plume. Undifferentiated magma directly intruded the shallow continental crust to form (ultramafic) rocks or breccia pipes, mainly composed of pyroxenite, gabbro, and syenite, with a small amount of diabase and granite visible. This was the main period for the formation of Wajilitag and Xiaohaizi granites, and the diagenetic age of the Halajun area (including porphyritic granite) is relatively late (Figure 10c). (4) In the middle of the Permian (fourth stage), the mantle plume shrunk gradually (Figure 10d), and the deep magma mixed with the crust to form a small amount of mafic dikes, nephelinites, and granites.

6. CONCLUSION

(1) The porphyritic granite had high K and Na content, high REE, and obvious Eu negative anomaly, and the zircon U−Pb age is 275.7 ± 1.0 Ma. The biotite monzogranite has a weakly positive Eu anomaly, and the zircon U−Pb age is 268.9 ± 1.4 Ma. The zircon Lu−Hf isotopes of the two indicate that the granites are related to the accumulation of deep magma and the periodic pulsation of the mantle plume.

(2) Granites are high-differentiation I-type granites and postcollisional granites, and porphyritic granite represents the lower limit of the regional metallogenic age, while biotite granite represents the end of the mantle plume activity. Porphyritic granites may be derived from the enriched mantle (i.e., ancient material recycling or modification), and biotite monzogranite may be derived from a small amount of depleted mantle, but mainly from the modification and recycling of preexisting crustal components.

■ ASSOCIATED CONTENT

Data Availability Statement

All data generated or analyzed during this study are included in this article.

■ AUTHOR INFORMATION

Corresponding Author

Zhengle Chen − *State Key Laboratory of Nuclear Resources and Environment, East China University of Technology, Nanchang 330013, China; Institute of Geomechanics, Chinese Academy of Geological Sciences, Beijing 100081, China*; Email: Chenzhengle@263.net

Authors

Zhuang Min − *State Key Laboratory of Nuclear Resources and Environment, East China University of Technology, Nanchang 330013, China; Institute of Geomechanics, Chinese Academy of Geological Sciences, Beijing 100081, China*; orcid.org/0000-0002-0706-2832

Jiayong Pan − *State Key Laboratory of Nuclear Resources and Environment, East China University of Technology, Nanchang 330013, China*

Qing Zhang − *Institute of Geomechanics, Chinese Academy of Geological Sciences, Beijing 100081, China*

Hailong Huo − *Institute of Geomechanics, Chinese Academy of Geological Sciences, Beijing 100081, China*

Fengbin Han − *Institute of Geomechanics, Chinese Academy of Geological Sciences, Beijing 100081, China*

Wengao Zhang − *Institute of Geomechanics, Chinese Academy of Geological Sciences, Beijing 100081, China*

Xiaohu Wang − *Institute of Geomechanics, Chinese Academy of Geological Sciences, Beijing 100081, China*

Yu Wu − *Beijing Research Institute of Uranium Geology, China National Nuclear Corporation, Beijing 100029, China*

Complete contact information is available at: https://pubs.acs.org/10.1021/acsomega.3c04415

https://doi.org/10.1021/acsomega.3c04415
ACS Omega 2023, 8, 47496−47509

Author Contributions

Z.C., Q.Z., and J.P. put forward the research direction; Z.M., H.H., and F.H. analyzed the data and wrote the paper; W.Z. and X.W. treated samples and performed experiments; Y.W. searched the literature. The authors also thank the journal reviewers and editors for their constructive comments on the manuscript.

Notes

The authors declare no competing financial interest.

■ ACKNOWLEDGMENTS

We thank Professor Greg Shellnut, Ren-Yu Zeng, and Zhong-Fu Jun for their encouragement and constructive comments of the manuscript. We would also like to thank the anonymous reviewers for their comments, which helped to improve the manuscript. This study is supported by the National Natural Science Foundation of China (grant no. 42172258), the second-level project of Geological Survey Project of China Geological Survey (nos. DD20221660-3 and DD20230293), the Joint Innovation Fund Project of China Uranium Industry Corporation Limited and State Key Laboratory of Nuclear Resources and Environment of East China University of Technology (no. NRE2021-01), the Guizhou Provincial Science and Technology Projects (Qiankehezhicheng [2021] 408), the Major project of Guizhou Bureau of Geology and Mineral Resources Exploration and Development(Qiandikuangkehe [2021] 1), the Science and Technology Foundation of Guizhou Province (Qian Ke He Ping Tai Ren Cai CXTD [2021] 007), and the Jiangxi Provincial Graduate Innovation Special Fund Project (no. YC2022-B178).

■ REFERENCES

(1) Han, B. F.; He, G. Q.; Wang, X. C.; Guo, Z. J. Late Carboniferous collision between the Tarim and Kazakhstan−Yili terranes in the western segment of the South TianShan Orogen, Central Asia, and implications for the Northern Xinjiang, western China. *Earth-Sci. Rev.* **2011**, *109*, 74−93.

(2) Li, X. J. Geological characteristics of the three rare minerals in the Keping continental margin basin of the Tianshan Mountains in southwest Xinjiang. *Western Prospecting Engineering* **2019**, *31*, 108−109 (in Chinese).

(3) Huang, H.; Zhang, Z. C.; Zhang, S.; Zhang, D. Y. Petrology and geochemistry of the Huoshibulake alkali feldspar granite plutonin Southwest Tianshan Moumntains, Xinjiang: Implications for petrogenesis, tectonic setting and mineralization. *Acta Petrol. Mineral* **2010**, *29*, 707−718 (in Chinese).

(4) Zou, S. Y.; Li, Z. L.; Song, B.; Ernst, R. E.; Li, Y. Q.; Ren, Z. Y.; Yang, S. F.; Chen, H. L.; Xu, Y. G.; Song, X. Y. Zircon U−Pb dating, geochemistry and Sr−Nd−Pb−Hf isotopes of the Wajilitag alkali mafic dikes, and associated diorite and syenitic rocks: Implications for magmatic evolution of the Tarim large igneous province. *Lithos* **2015**, *212−215*, 428−442.

(5) Zhu, S. Z.; Huang, X. L.; Yang, F.; He, P. L. Petrology and geochemistry of early Permian mafic−ultramafic rocks in the Wajilitag area of the southwestern Tarim Large Igneous Province: Insights into Fe-rich magma of mantle plume activity. *Lithos* **2021**, 398−399.

(6) Li, Y. Q.; Li, Z. L.; Chen, H. L.; Yang, S. F.; Yu, X. Mineral characteristics and metallogenesis of the Wajilitag layered mafic−ultramafic intrusion and associated Fe−Ti−V oxide deposit in the Tarim large igneous province, northwest China. *J. Asian Earth Sci.* **2012**, *49*, 161−174.

(7) Zhang, C. L.; Zhou, G.; Wang, H. Y.; Dong, Y. G.; Ding, R. F. A review on two types of mantle domains of the Permian large igneous province in Tarim and the western section of Central Asian orogenic belt. *Geol. Bull. China* **2010**, *29* (6), 779−794 (in Chinese).

(8) Cao, J.; Wang, C. Y.; Xu, Y. G.; Xing, C. M.; Ren, M. H. Triggers on sulfide saturation in Fe−Ti oxide-bearing, mafic-ultramafic layered intrusions in the Tarim large igneous province, NW China. *Miner. Deposita* **2017**, *52*, 471−494.

(9) Ni, K. Discovery of the Mazaertagh V-Ti Magnetite Deposit in Western Tarim and its significance tiltle in English. *Adv. Earth Sci.* **2012**, *27*, 236−239 (in Chinese).

(10) Cao, J.; Xu, Y. G.; Xing, C. M.; Huang, X. L.; Li, H. Y. Origin of the Early Permian granitic plutons from the Piqiang region in the northern Tarim Block: Implications for the origin of A-type granites of the Tarim large igneous province. *Acta Petrol. Sin.* **2013**, *29* (10), 3336−3352 (in Chinese).

(11) Huang, H.; Zhang, Z. C.; Kusky, T.; Santosh, M.; Zhang, S.; Zhang, D. Y.; Liu, J. L.; Zhao, Z. D. Continental vertical growth in the transitional zone between South Tianshan and Tarim, western Xinjiang, NW China: Insight from the Permian Halajun A1-type granitic magmatism. *Lithos* **2012**, *155*, 49−66.

(12) Zhang, C. J.; Wang, H. J.; Shi, G. H. The Geological features and mine prospecting significance of Puchang ilmenite mine in Atushi, Xinjiang. *Xinjiang Geology* **2013**, *31*, 29−33 (in Chinese).

(13) Cao, J.; Wang, X.; Tao, J. Petrogenesis of the Piqiang mafic-ultramafic layered intrusion and associated Fe-Ti-V oxide deposit in Tarim Large Igneous Province, NW China. *Int. Geol. Rev.* **2019**, *61*, 2249−2275.

(14) Zhang, D.; Zhang, Z.; Huang, H.; Cheng, Z. G.; Charlier, B. Petrogenesis and metallogenesis of the Wajilitag and Puchang Fe-Ti oxide-rich intrusive complexes, northwestern Tarim Large Igneous Province. *Lithos* **2018**, *304−307*, 412−435.

(15) Cao, J.; Tao, J.; Wang, X. SHRIMP Zircon U-Pb Ages of the Wajilitag Igneous Complex: Constraints on the Origin of A-type Granitoids in the Tarim Large Igneous Province, NW China. *Acta Geol. Sin.* **2017**, *91* (6), 2318−2320.

(16) Zhang, D.; Zhang, Z.; Huang, H.; Encarnación, J.; Zhou, N. W.; Ding, X. X. Platinum-group elemental and Re−Os isotopic geochemistry of the Wajilitag and Puchang Fe−Ti−V oxide deposits, northwestern Tarim Large Igneous Province. *Ore Geol. Rev.* **2014**, *57*, 589−601.

(17) Cao, J. *Origin of the Fe-Ti oxide mineralization and the host mafic-ultramafic layered intrusions in the Tarim large igneous province, NW China (in Chinese)*; Graduate University of Chinese Academy of Sciences (Guangzhou Institute of Geochemistry), 2015.

(18) Zhang, C. L.; Li, H. K.; Santosh, M.; Li, Z. X.; Zou, H. B.; Wang, H. Y.; Ye, H. M. Precambrian evolution and cratonization of the Tarim Block, NW China: Petrology, geochemistry, Nd-isotopes and U−Pb zircon geochronology from Archaean gabbro-TTG−potassic granite suite and Paleoproterozoic metamorphic belt. *J. Asian Earth Sci.* **2012**, *47*, 5−20.

(19) Zhang, D. Y.; Zhou, T. F.; Yuan, F.; Jowitt, S. M.; Fan, Y.; Liu, S. Source, evolution and emplacement of Permian Tarim Basalts: Evidence from U−Pb dating, Sr−Nd−Pb−Hf isotope systematics and whole rock geochemistry of basalts from the Keping area, Xinjiang Uygur Autonomous region, northwest China. *J. Asian Earth Sci.* **2012**, *49*, 175−190.

(20) Chen, M. M.; Tian, W.; Zhang, Z. L.; Pan, W. Q.; Song, Y. Geochronology of the Permian basic-intermediate-acidicmagma suite from Tarim, Northwest China and its geological implications. *Acta Petrol. Sin.* **2010**, *26* (2), 559−572 (in Chinese).

(21) Yu, J. C.; Mo, X. X.; Dong, G. C.; Yu, X. H.; Xing, F. C.; Li, Y.; Huang, X. K. Felsic volcanic rocks from northern Tarim, NW China: Zircon U-Pb dating and geochemical characteristics. *Acta Petrol. Sin.* **2011**, *27* (7), 2184−2194 (in Chinese).

(22) He, W. Y.; Li, J. H.; Qian, X. L.; Zheng, D. M. Analysis of fault structures in the Kalpin fault uplift, Tarim basin. *Geol. China* **2002**, *29* (10), 37−43 (in Chinese).

(23) Zhang, C. L.; Zou, H. B. Permian A-type granites in Tarim and western part of Central Asian Orogenic Belt (CAOB): Genetically related to a common Permian mantle plume? *Lithos* **2013**, *172−173*, 47−60.

https://doi.org/10.1021/acsomega.3c04415
ACS Omega 2023, 8, 47496−47509

(24) Zhang, C. L.; Li, Z. X.; Li, X. H.; Xu, Y. G.; Zhou, G.; Ye, H. M. A Permian large igneous province in Tarim and Central Asian orogenic belt, NW China: Results of a ca. 275 Ma mantle plume? *Geol. Soc. Am. Bull.* **2010**, *122*, 2020−2040.
(25) Zhang, D. Y.; Zhang, Z. C.; Santosh, M.; Cheng, Z. G.; Huang, H.; Kang, J. L. Perovskite and baddeleyite from kimberlitic intrusions in the Tarim large igneous province signal the onset of an end-Carboniferous mantle plume. *Earth Planet. Sci. Lett.* **2013**, *361*, 238−248.
(26) Wiedenbeck, M.; Alle, P.; Corfu, F.; Griffin, W. L.; Meier, M.; Oberli, F.; von Quadt, A.; Roddick, J. C.; Spiegel, W. Three Natural Zircon Standards for U-Th-Pb, Lu-Hf, Trace Element and REE Analyses. *Geostand. Geoanal. Res.* **1995**, *19*, 1−23.
(27) Jackson, S. E.; Pearson, N. J.; Griffin, W. L.; Belousova, E. A. The application of laser ablation-inductively coupled plasma-mass spectrometry to in situ U−Pb zircon geochronology. *Chem. Geol.* **2004**, *211*, 47−69.
(28) SláMa, J.; KošLer, J.; Condon, D. J.; Crowley, J. L.; Gerdes, A.; Hanchar, J. M.; Horstwood, M. S. A.; Morris, G. A.; Nasdala, L.; Norberg, N.; Schaltegger, U.; Schoene, B.; Tubrett, M. N.; Whitehouse, M. J. Plešovice zircon—A new natural reference material for U−Pb and Hf isotopic microanalysis. *Chem. Geol.* **2008**, *249*, 1−35.
(29) Liu, Y.; Gao, S.; Hu, Z.; Gao, C.; Zong, K.; Wang, D. Continental and Oceanic Crust Recycling-induced Melt-Peridotite Interactions in the Trans-North China Orogen: U-Pb Dating, Hf Isotopes and Trace Elements in Zircons from Mantle Xenoliths. *J. Petrol.* **2010**, *51*, 537−571.
(30) Liu, Y.; Hu, Z.; Zong, K. Q.; Gao, C. G.; Gao, S.; Xu, J.; Chen, H. H. Reappraisement and refinement of zircon U-Pb isotope and trace element analyses by LA-ICP-MS. *Chin. Sci. Bull.* **2010**, *55*, 1535−1546.
(31) Vermeesch, P. IsoplotR: A free and open toolbox for geochronology. *Geosci. Front.* **2018**, *9*, 1479−1493.
(32) Sderlund, A. U.; Jonathan Patchett, A. P.; Vervoort, B. J. D.; Isachsen, A. C. E. The ^{176}Lu decay constant determined by Lu−Hf and U−Pb isotope systematics of Precambrian mafic intrusions. *Earth Planet. Sci. Lett.* **2004**, *219*, 311−324.
(33) Blichert-Toft, J.; AlbarèDe, F. The Lu-Hf isotope geochemistry of chondrites and the evolution of the mantle-crust system. *Earth Planet. Sci. Lett.* **1998**, *154* (1−2), 243−258.
(34) Griffin, W. L.; Pearson, N. J.; Belousova, E.; Jackson, S. E.; van Achterbergh, E.; O'Reilly, S. Y.; Shee, S. R. The Hf isotope composition of cratonic mantle: LA-MC-ICPMS analysis of zircon megacrysts in kimberlites. *Geochim. Cosmochim. Acta* **2000**, *64*, 133−147.
(35) Hou, K. J.; YH, L.; Zou, T. R.; Qu, X. M.; Shi, Y. R.; Xie, G. Q. Laser ablation-MC-ICP-MS technique for Hf isotope microanalysis of zircon and its geological applications. *Acta Petrol. Sin.* **2007**, *23* (10), 2595−2604 (in Chinese).
(36) Huang, G.; Pan, J.; Xia, F.; Yan, J.; Zhang, C.; Wu, D.; Liu, Y. Provenance of uranium mineralization of the Yuqia area, Northwest China: Constraints from detrital zircon U-Pb geochronology and Hf isotopes. *J. Earth Sci.* **2022**, *33*, 1549−1570.
(37) Zou, S. Y. *Magmatic events in the late stage and its evolution of Tarim lage igneous province (in Chinese)*. Zhejiang University, 2016.
(38) Taylor, S. R.; Mclennan, S. M. *The Continental Crust: Its Composition and Evolution*; Blackwell: Oxford, 1985; p 312.
(39) Peccerillo, A.; Taylor, S. R. Geochemistry of eocene calc-alkaline volcanic rocks from the Kastamonu area, Northern Turkey. *Contrib. Mineral. Petrol.* **1976**, *58*, 63−81.
(40) Rickwood, P. C. Boundary lines within petrologic diagrams which use oxides of major and minor elements. *Lithos* **1989**, *22*, 247−263.
(41) Shellnutt, G. J.; Wang, K. L.; Zellmer, G. F.; Iizuka, Y.; Jahn, B. M.; Pang, K. N.; Qi, L.; Zhou, M. F. Three Fe-Ti oxide ore-bearing gabbro-granitoid complexes in the Panxi region of the permian emeishan large igneous province, SW China. *Am. J. Sci.* **2011**, *311*, 773−812.
(42) Boynton, W. V. Cosmochemistry of the Rare Earth Elements. In *Rare Earth Element Geochemistry. Developments in Geochemistry*; Ins Henderson, P. Ed., 1984; pp. 63−114.
(43) Sun, S. S.; Mcdonough, W. F. *Chemical and isotopic systematics of oceanic basalts: Implications for mantle composition and processes*; Geological Society, London, Special Publications, 1989; Vol. *42*, pp. 313−345.
(44) Ge, R.; Zhu, W.; Wu, H.; Zheng, B. H.; Zhu, X. Q.; He, J. W. The Paleozoic northern margin of the Tarim Craton: Passive or active? *Lithos* **2012**, *142*−*143*, 1−15.
(45) Chen, H. L.; Yang, S. F.; Jia, C. Z.; Dong, C. W.; Wei, G. Q. Confirmation of Permian intermediate-acid igneous rock zone and a new understanding of tectonic evolution in the northern part of the Tarim basin. *Acta Mineral. Sin.* **1998**, *18* (3), 370−376 (in Chinese).
(46) Rubatto, D.; Gebauer, D. *Use of cathodoluminescence for U-Pb zircon dating by ion microprobe: Some examples from the Western Alps*; Springer: Berlin Heidelberg, 2000; *15*, 373−400.
(47) Wu, F. Y.; Li, X. H.; Zheng, Y. F.; Gao, S. Lu-Hf isotopic systematics and their applications in petrology. *Acta Petrol. Sin.* **2007**, *23* (2), 185−220 (in Chinese).
(48) Wu, Y. B.; Zheng, Y. F. Zircon genetic mineralogy and its constraints on the interpretation of U-Pb age. *Sci. Bull.* **2004**, 1589−1604 (in Chinese).
(49) Zhang, C. L.; Xu, Y. G.; Li, Z. X.; Wang, H. Y.; Ye, H. M. Diverse Permian magmatism in the Tarim Block, NW China: Genetically linked to the Permian Tarim mantle plume? *Lithos* **2010**, *119*, 537−552.
(50) Zhou, L. X.; Hu, S. L.; Wang, L. G.; Li, Y. J.; Huang, Z. B.; Zhu, H. Y.; Zhao, Y.; Liu, Y. L. The age of Piqiang gabbroid, NW margin of Tarim Basin, NW China. *Chin. J. Geol.* **2010**, *45*, 1057−1065 (in Chinese).
(51) Zhang, D. Y.; Zhang, Z. C.; Mao, J. W.; Huang, H.; Cheng, Z. G. Zircon U−Pb ages and Hf−O isotopic signatures of the Wajilitag and Puchang Fe−Ti oxide−bearing intrusive complexes: Constraints on their source characteristics and temporal−spatial evolution of the Tarim large igneous province. *Gondwana Res.* **2016**, *37*, 71−85.
(52) Zhang, D. Y.; Zhang, Z.; Mao, J.; Huang, H.; Cheng, Z. Zircon U−Pb ages and Hf−O isotopic signatures of the Wajilitag and Puchang Fe−Ti oxide−bearing intrusive complexes: Constraints on their source characteristics and temporal−spatial evolution of the Tarim large igneous province. *Gondwana Res.* **2016**, *37*, 71−85.
(53) Yu, X.; Chen, H. L.; Yang, S. F.; Li, Z. L.; Wang, Q. H.; Lin, X. B.; Xu, Y.; Luo, J. C. Geochemical features of Permian basalts inTarim Basin and compared with Emeishan LlP. *Acta Petrol. Sin.* **2009**, *25* (6), 1492−1498 (in Chinese).
(54) Zhang, D. Y. *Mafic-Ultramafic plutons and their metallogenic effects in Tarim Great Igneous Province (in Chinese)*; China University Geosciences (Beijing), 2014
(55) Chappell, B. W.; White, A. J. R. Two contrasting granite type. *Pac. Geol.* **1974**, *8*, 173−174.
(56) Miller, C. F. Are Strongly Peraluminous Magmas Derived from Pelitic Sedimentary Sources? *J. Geol.* **1985**, *93* (6), 673−689.
(57) Pichavant, M.; Montel, J. M.; Richard, L. R. Apatite solubility in peraluminous liquids: Experimental data and an extension of the Harrison-Watson model. *Geochim. Cosmochim. Acta* **1992**, *56*, 3855−3861.
(58) Li, X. H.; Li, W.-X.; Li, Z.-X. On the genetic classification and tectonic implications of the Early Yanshanian granitoids in the Nanling Range, South China. *Chin. Sci. Bull.* **2007**, *52* (14), 1873−1885.
(59) Whalen, J. B.; Currie, K. L.; Chappell, B. W. A-type granites: Geochemical characteristics, discrimination and petrogenesis. *Contrib. Mineral. Petrol.* **1987**, *95*, 407−419.
(60) Eby, G. N. Chemical subdivision of the A-type granitoids: Petrogenetic and tectonic implications. *Geology* **1992**, *20*, 641.
(61) Li, Y. Q. *Study on magma dynamics and ore potential of the early Permian Tarim Large Igneous Province (in Chinese)*; Zhejiang University, 2013.

https://doi.org/10.1021/acsomega.3c04415
ACS Omega 2023, 8, 47496−47509

(62) Zhang, C. L.; Li, X. H.; Li, Z. X.; Ye, H. M.; Li, C. N. A Permian layered intrusive complex in the western Tarim block, northwestern China: Product of a ca. 275Ma mantle plume? *J. Geol.* **2008**, *116*, 269−287.
(63) Xiao, W.; Han, C. M.; Yuan, C.; Yuan, C.; Sun, M.; Lin, S. F.; Chen, H. L.; Li, Z. L.; Li, J. L.; Sun, S. Middle Cambrian to Permian subduction-related accretionary orogenesis of Northern Xinjiang, NW China: Implications for the tectonic evolution of central Asia. *J. Asian Earth Sci.* **2008**, *32*, 102−117.
(64) Xiao, W. J.; Windley, B. F.; Huang, B. C.; Han, C. M.; Yuan, C.; Chen, H. L.; Sun, M.; Sun, S.; Li, J. L. End-Permian to mid-Triassic termination of the accretionary processes of the southern Altaids: Implications for the geodynamic evolution, Phanerozoic continental growth, and metallogeny of Central Asia. *Int. J. Earth Sci.* **2009**, *98*, 1189−1217.
(65) Jiang, C. Y.; Zhang, P. B.; Lu, D. R.; Bai, K. Y. Petrogenesis and magma source of the ultramafic rocks at Wajilitag region, western Tarim Plate in Xinjiaug. *Acta Petrol. Sin.* **2004**, *20* (6), 1433−1444 (in Chinese).
(66) Tian, W.; Campbell, I. H.; Allen, C. M.; Guan, P.; Pan, W. Q.; Chen, M. M.; Yu, H. J.; Zhu, W. P. The Tarim picrite−basalt−rhyolite suite, a Permian flood basalt from northwest China with contrasting rhyolites produced by fractional crystallization and anatexis. *Contrib. Mineral. Petrol.* **2010**, *160*, 407−425.
(67) Yu, X.; Yang, S. F.; Chen, H. L.; Chen, Z. Q.; Li, Z. L.; Batt, G. E.; Li, Y. Q. Permian flood basalts from the Tarim Basin, Northwest China: SHRIMP zircon U−Pb dating and geochemical characteristics. *Gondwana Res.* **2011**, *20*, 485−497.
(68) Han, Y.; Zhao, G.; Cawood, P. A.; Sun, M.; Liu, Q.; Yao, J. L. Plume-modified collision orogeny: The Tarim−western Tianshan example in Central Asia. *Geology* **2019**, *47*, 1001−1005.

https://doi.org/10.1021/acsomega.3c04415
ACS Omega 2023, 8, 47496−47509